Thick $BaTiO_3$ epitaxial films integrated on Si by RF sputtering for electro-optic modulators in Si photonics

Agham B. Posadas[a], Hyoju Park[b,c], Marc Reynaud[a], Wei Cao[d], Jamie D. Reynolds[d], Wei Guo[a], Vadivukkarasi Jeyaselvan[d], Ilya Beskini[a], Goran Z. Mashanovich[d], Jamie H. Warner[b,c] and Alexander A. Demkov[a]*

[a]Department of Physics, The University of Texas at Austin, Austin, TX 78712, USA

[b]Materials Science and Engineering Program and Texas Materials Institute, The University of Texas at Austin, Austin, Texas 78712, United States

[c]Walker Department of Mechanical Engineering, The University of Texas at Austin, Austin, Texas 78712, United States

[d]Optoelectronics Research Centre, Faculty of Engineering and Physical Sciences, University of Southampton, Southampton, United Kingdom

KEYWORDS

Pockels effect, electro-optic modulator, silicon photonics, barium titanate, waveguides, epitaxial growth, off-axis sputtering

ABSTRACT

Thick epitaxial $BaTiO_3$ films ranging from 120 nm to 1 μm were grown by off-axis RF magnetron sputtering on $SrTiO_3$-templated silicon-on-insulator (SOI) substrates for use in electro-optic applications, where such large thicknesses are necessary. The films are of high quality, rivaling those grown by molecular beam epitaxy (MBE) in crystalline quality, but can be grown ten times faster. Extraction of lattice parameters from geometric phase analysis of atomic resolution scanning transmission electron microscopy images revealed how the in-plane and out-of-plane lattice spacings of sputtered $BaTiO_3$ changes as a function of layer position within a thick film. Our results indicate that, compared to molecular beam epitaxy, sputtered films retain their out-of-plane polarization (c-axis) orientation for larger thicknesses. We also find an unusual re-transition from in-plane polarization (a-axis) to out-of-plane polarization (c-axis), along with an anomalous lattice expansion, near the surface. We also studied a method of achieving 100% a-axis oriented films using a two-step process involving amorphous growth and recrystallization of a seed layer followed by normal high temperature growth. While this method is successful in achieving full a-axis orientation even at low thicknesses, the resulting film has a large number of voids and misoriented grains. Electro-optic measurement using a transmission setup of a sputtered BTO film grown using the optimized conditions yields an effective Pockels coefficient as high as 183 pm/V. A Mach-Zehnder modulator fabricated on such films exhibits phase shifting with an equivalent Pockels coefficient of 157 pm/V. These results demonstrate that sputtered BTO thick films can be used for integrated electro-optic modulators for Si photonics.

1. Introduction

Barium titanate ($BaTiO_3$ or BTO) thin films have been the subject of renewed interest in the past decade because of its strong linear electro-optic (Pockels) response.[1-3] The relative ease of growing it in epitaxial form on Si now makes it possible to integrate electro-optic (EO) modulators based on BTO with Si photonics.[4-5] Films for optical applications require relatively large thickness (0.3 to 1 μm) while maintaining high crystalline quality and smooth surfaces. Qiu et al.[6] showed using Landau-Devonshire theory that the Pockels coefficient of a BTO thin film scales with film thickness for very thin films and only reaches the maximum bulk value when the thickness exceeds 100 nm. Kormondy et al.[7] showed that the film microstructure can also strongly affect the measured Pockels coefficient. Films that have higher porosity have reduced Pockels coefficients and that the degree of porosity appears to be primarily related to growth rate, which is well-established in the field of thin film growth.[8] Methods to prepare dense, high crystallinity, thick films of BTO in a straightforward and reasonably fast manner are therefore crucial for industrial scale electro-optic applications of BTO.

Epitaxial BTO thick films grown on MgO single crystal substrates are well-established, with a ~~lot of~~ pioneering work by the Wessels group at Northwestern University.[9-10] In the last decade, it was recognized by researchers in the field that BTO thin-film-based EO modulators are needed in order to realize bandwidths on the order of 100 GHz for the highest data-rate transmission of 400 Gbit/s, which is beyond the capabilities of $LiNbO_3$-based devices.[11] Major milestones in the demonstration of the capability of BTO-based EO modulators were reported by Liu and Wessels using Si_3N_4 waveguides on BTO/MgO in 2013;[12] by Abel et al. at IBM Zurich in 2013 using Si waveguides on BTO/Si^2; and by Xiong et al. at Yale University in 2014.[13]

Thick films (>200 nm) of BTO have been grown previously using a variety of methods, most notably by sol-gel, metal-organic chemical vapor deposition, sputtering and pulsed laser deposition (PLD).[14] Thick films were usually grown at a very fast rate (on the order of 100 A/min or more) and usually deposited amorphous and recrystallized. Growth of BTO using molecular beam epitaxy (MBE) produces high quality epitaxial films but the process is relatively slow.[15] Among these methods, radio frequency (RF) magnetron sputtering is considered here due its medium deposition rate, large area uniformity, and compatibility with industrial mass production. Using standard on-axis RF magnetron sputtering from a BTO target can be problematic because of the creation of negative oxygen ions (O^-, O^{2-}). These negative ions can have sufficient kinetic energy from the target self-bias field to bombard the substrate and cause preferential re-sputtering, which significantly alters the stoichiometry, or even etch the growing film.[16] To avoid this effect, we employ the off-axis geometry, where the substrate is not along the target axis.

The RF sputtering of BTO was first reported in 1971[17] but researchers were mainly growing amorphous or polycrystalline films at that time, mainly for bulk dielectric applications. It was not until the late 1980s when the sputter deposition of BTO began to be studied thoroughly and systematically with the goal of getting the highest quality films as grown. This coincided with the wide availability of single crystal $SrTiO_3$ (STO) and MgO substrates, as well as technological advancements in vacuum technology. Lee et al.[18] studied the effect of gas pressure and gas composition on the orientation, lattice parameters, and crystallite size of the grown BTO films. They found that low pressures (<5 mTorr) favor the growth of 001/100-oriented films, while higher pressures (>30 mTorr) tend to favor 110-oriented growth, with 111-oriented growth in between. Oxygen content on the other hand also appears to be important. Too much oxygen

tends to produce random polycrystalline films while too little oxygen renders the film amorphous. An intermediate oxygen fraction of ~30% seems to be the most suitable for getting 001/100-oriented films. Lee et al. also studied the effect of substrate temperature, and found that the film becomes amorphous at 100°C and random polycrystalline up to 500°C [18]. Beyond this temperature, highly oriented films tend to be formed. A similar study on the effect of pressure on epitaxial films was recently reported by Lyu et al.[19] on PLD-grown BTO. They found that higher pressures (100 mbar) of oxygen produced a large amount of voids while lower pressure (10 mbar) favors homogenous and smooth films. Concurrently, low pressure-grown films are 001-oriented (c-axis oriented) while high pressure grown films are 100-oriented (a-axis oriented). These observations are in line with the predictions of the Thornton structural zone model, including further modifications to account for mean kinetic energy of the arriving species.[20-21] With a melting point (T_m) of 1612°C for BTO, it is expected that growth temperatures greater than 500°C ($T/T_m > 0.4$) are needed to obtain flat, highly-oriented films.

A more recent systematic study of on-axis RF sputtering of BTO was reported by Vargas et al. in 2015.[22] They studied the effect of RF power and total pressure on the quality of films grown. One of their key findings is that beyond a power density of 4 W/cm^2, the Ba/Ti ratio begins to diverge rapidly away from 1, becoming as high as 3 for a power density of 20 W/cm^2. In addition, they also observed significant substrate etching due to re-sputtering at power densities as low as 5 W/cm^2, and progressively increasing non-uniformity as power increases. This reveals that power density should be kept as low as possible, particularly if growing using the on-axis geometry, where the substrate and target face each other directly.

BTO grown epitaxially in the 100/001 orientation can choose to grow either c-axis oriented (polarization out of plane) or a-axis oriented (polarization in plane) depending on lattice

matching and thermal expansion differences with the substrate. Because the MgO lattice constant is larger than the c lattice parameter of BTO, one expects the BTO to grow a-oriented (c-axis in-plane). However, due to thermal expansion mismatch with MgO, BTO films are more likely to grow c-oriented unless cooled very slowly.[23-24] On the other hand, when grown on STO, which has similar thermal expansion as BTO, the smaller in-plane lattice constant of STO should cause BTO to grow c-oriented. Electrostatic boundary conditions should eventually force the c-oriented BTO to become a-oriented.[25-26] The point at which this happens appears to vary widely though and depends strongly on the deposition method, growth rate, and film quality. MBE growth, which is quite slow (0.2-0.4 nm/min) results in the c-to-a transition occurring after a thickness of 25 nm, with full a-orientation typically reported by 130 nm.[2,26-27] Sputtering or PLD growth retains the c-orientation for larger thickness, with up to 200 nm of fully c-oriented films reported,[28] or even larger if a conductive buffer layer like $LaNiO_3$ is used.[29-31] A study of the critical thickness for BTO relaxation on STO using PLD was done by Kawai et al.[32] Their key finding is that a growth rate of 0.6 nm/min results in the film being c-oriented but relaxed, while growth rates of 2.4 nm/min results in the film remaining fully strained to STO, for a BTO film thickness of 50 nm.

When growing on STO-buffered Si, the thickness of the STO layer also seems to be important. Hsu et al.[33] performed a study of the effect of STO thickness on the BTO grown by MBE on STO/Si. A 100 nm BTO film remains c-oriented when grown by MBE on thick (40 nm) STO, while the same thickness of BTO becomes a-oriented when grown on thin (5 nm) STO. A notable exception is a recent report by Merckling et al.[34] where the c-to-a transition did not occur at the expected thickness of 25 nm for MBE growth but at closer to 150 nm thickness. They attribute this to the different way they grow STO on Si (fully crystalline as deposited).

MBE-grown epitaxial films of BTO on Si have been proven to have sufficient quality for electro-optic applications but have typically been grown routinely only to 150 nm thickness or less for practical reasons because of the very slow growth rates and the drift in fluxes with MBE over prolonged runs. As discussed above, growth of thick epitaxial films (0.5-2 μm) has been demonstrated on MgO single crystal substrates with sufficient optical quality using sputtering and PLD, but thick optical quality films on STO/Si are not as common. Here, we report on the growth of epitaxial films up to 1 μm thick using off-axis RF sputtering on STO/Si. We show that this off-axis configuration allows one to obtain MBE-quality electro-optically active films with growth rates about ten times faster, making the fabrication of micron-thick epitaxial films on Si for electro-optic applications readily achievable and manufacturable.

2. Experimental Section

2.1 Growth

We use off-axis RF magnetron sputtering to deposit BTO films epitaxially on Si with up to 1 μm in thickness. The films were grown in a custom hybrid deposition system manufactured by DCA Instruments, which combines both oxide MBE and RF sputtering in the same chamber. The sputtering target is a stoichiometric 2-in. diameter ceramic target of $BaTiO_3$ from Plasmaterials. The sputtering is carried out by using a process gas that is a mixture of Ar and O_2 with a flow ratio of 70:30. The total pressure is kept constant at 10-20 mTorr as measured by a capacitance manometer using upstream flow control of the individual mass flow rates. We use a low forward RF power of 45 W (2.2 W/cm^2 power density) for the sputtering growth. Prior to each growth, the target is pre-sputtered without a sample for 20 minutes to ensure the target surface is clean and surface composition is constant. Samples were grown at a substrate height of 4.9 cm above

the sputtering gun axis; the sputtering gun lateral position was first adjusted until the correct film stoichiometry was obtained. Details of the gun position optimization are described in the Supporting Information. These two distances are illustrated in Fig. 1a, which shows a schematic of the off-axis geometry between the sputtering gun and the sample stage.

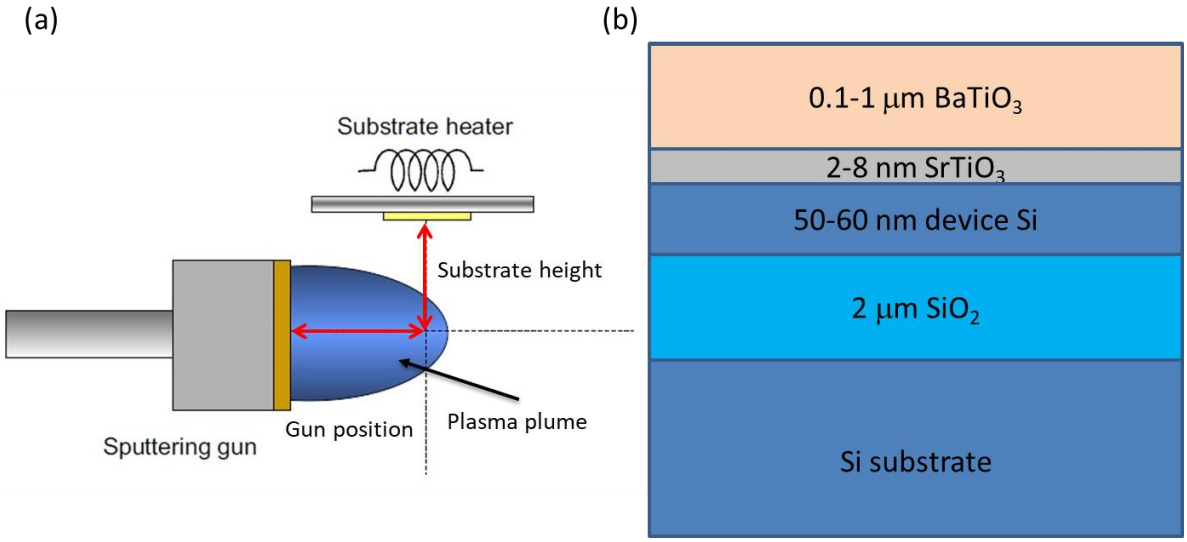

Figure 1. (a) Schematic of the off-axis sputtering configuration showing the two distance parameters (substrate height and gun position) that can be adjusted. Note that the substrate is not located along the gun axis where the main part of the plasma is concentrated. (b) Layer structure of the samples. The device Si layer of the SOI wafer is thinned down then STO is grown by MBE followed by BTO growth by off-axis sputtering. The ~3 nm SiO_2 interlayer that forms between STO and device Si during BTO deposition is not shown. The drawing is not to scale.

BTO films ranging from 120 nm to 1 μm in thickness were deposited at a fixed substrate temperature of 700°C by off-axis RF sputtering on silicon-on-insulator (SOI) substrates with an STO template layer epitaxially grown by MBE on the device Si layer. This substrate temperature

correrspponds to $T/T_m = 0.50$ and is expected to produce dense columnar growth according to the Thornton structural zone model.[20-21] The device Si layer of the SOI wafer was first thinned down to 50-60 nm from its original thickness of 220 nm by oxidation and HF etching. After the SOI wafer is degreased by sonication in acetone, isopropanol, and deionized water, the native oxide is removed and an STO template layer is grown using the process described in Choi et al.[35] A schematic of the overall film structure is shown in Fig. 1b. The STO template layer thickness was varied from 2 to 8 nm to study how it affects the BTO strain relaxation and to determine the optimum template layer thickness. The effect of BTO film thickness on the BTO surface and bulk crystalline quality and on the crystallographic orientation was also determined. Two-step growth processes involving growing either an amorphous or poorly crystallized seed layer that is later annealed, followed by a second growth on top of the recrystallized layer, were also studied in order to maximize the a-oriented volume fraction, which is important in electro-optic applications utilizing transmission through the film or using planar waveguides.

2.2. Structural characterization

All films grown were analyzed by x-ray diffraction (XRD) using a Rigaku Ultima IV diffractometer with Cu Kα radiation and a Ge two-bounce monochromator for the incident beam. We measured a relatively fast (7.5°/min) wide range scan to determine if there are other BTO orientations present, especially the 110 orientation, which is an indication of the presence of polycrystalline BTO. We also performed a high resolution measurement of the 200 Bragg region of BTO to determine precisely the relative amounts of c- and a-axis orientation present in the films. Finally, rocking curves were performed on the main 200 peak to quantify the overall bulk crystallinity of the films. In-plane diffraction scans utilizing the in-plane detector arm of the

Rigaku Ultima IV were performed for a selected number of films to confirm that the BTO long c-axis is in-plane.

The growth rate for the optimum source-target geometry was determined by measuring the thickness of a film grown for a set amount of time (40 min) using x-ray reflectivity (XRR). The XRR data is modeled and the best fit to the observed signal is found to correspond to a thickness of 82.0 nm revealing a growth rate of 2.05 nm/min for the optimized source-target geometry. The XRR data and simulation for the calibration sample is shown in the Supporting Information (Fig. S1). X-ray photoelectron spectroscopy (XPS) was used to check the film stoichiometry. Details of the XPS experimental setup are found in the Supporting Information.

The cross-sectional samples for scanning transmission electron microscopy (STEM) were fabricated using a Scios 2 HiVac focused ion beam system from Fisher Scientific. Annular dark-field STEM (ADF-STEM) was performed using a JEOL NEOARM equipped with a probe corrector for STEM, operated at an accelerating voltage of 200 kV. To precisely measure the lattice parameter of BTO while minimizing the error from camera scanning, ADF-STEM images were carefully calibrated using the silicon lattice spacing under the BTO/STO layer. The local in-plane and out-of-plane lattice constants were determined from the average of around twenty spacings of Ba atoms from each sampled region in Figure 7 with the atomically resolved ADF-STEM images. Geometric phase analysis (GPA) was performed in Digital Micrograph using Koch's FRWR tools plugin,[36] which is based on the methods of Hytch et al.[37] Based on the calculated strain of GPA maps along the in-plane (ε_{xx}) and out-of-plane (ε_{yy}) directions with the selected G-vector of 3.999 Å, which is the median of a-axis and c-axis, the relative displacement was calculated by the product of the strain value with the inverse of the G-vector (real spacing) used for GPA maps. Strained lattice parameters are calculated as the relative displacement plus

3.999 Å. The converted lattice parameters from GPA analysis match those obtained from the actual averaged local lattice spacing measurements from the high-resolution STEM images.

2.3. Electro-optic characterization

For electro-optic characterization, patterned tungsten metal pads are deposited on the BTO using photolithography and lift-off to a thickness of about 300 nm. The separation between the tungsten pads is 10 μm. The measurements are performed at room temperature using the same experimental setup as in Reynaud et al.[38] A New Focus TLB 6800 LN 1550 nm diode laser is used in transmission mode and focused in the gap between two tungsten electrical contacts. A 35 V D.C. voltage is applied to the electrical contacts via a Keithley B2902A Source/Measure Unit, while a 5 V A.C. voltage is applied via an Ametek Signal Recovery Model 7270 DSP Lock-In Amplifier at a frequency of 17.3 kHz. The light's polarization is modulated in the BTO film between the contacts by the electric fields before being relinearized by a quarter wave plate with its polarization orientation being shifted. Then, the signal is detected with a Femto OE-200-IN2 photodetector, which is connected to both the Keithley and Ametek unit. The Keithley is used to measure the direct power while the Ametek is used to measure the modulation in the power, from which the Pockels response is extracted.

In order to verify the electro-optic response, we also fabricated Mach-Zehnder modulator (MZM) structures on the sputtered BTO films. Polycrystalline silicon-rich silicon nitride (SiN_x) with a thickness of 450 nm was first deposited on top of the 300 nm BTO layer using plasma-enhanced chemical vapor deposition (PECVD). Strip waveguides were then patterned by e-beam lithography and etched in an inductively coupled plasma etching (ICP) tool. Both sides of the waveguide are fully etched to exposed BTO and the metal electrodes are then deposited by

evaporation and patterned by lift-off. The metal layer contains a Ti/Au stack with 20 and 300 nm thickness, respectively. In the fabricated MZM device, the electrode length is 500 μm along the waveguide and its width is 100 μm. The electrode inner edge is 2.6 μm from the waveguide center, resulting in a total metal contact separation of 5.2 μm.

3. Results and Discussion

3.1. Effect of STO template layer thickness

When growing on Si, BTO requires a template layer of STO in order to grow epitaxially, since BTO cannot be nucleated directly on Si without interfacial reactions.[39] The discovery by McKee et al. in 1998 of a way to epitaxially nucleate STO on Si directly by MBE has opened up the possibility of integrating other perovskite materials on Si.[40-41] A typical process involves first removing the surface SiO_2 and then depositing 0.5 monolayer of Sr metal in an MBE chamber. This Sr sub-monolayer prevents Si oxidation during the initial nucleation of STO.[42] A thin (1-4 nm), barely crystalline STO layer is then deposited at low temperature (<300°C) with the correct stoichiometric ratio of Sr and Ti in the presence of modest oxygen pressure (10^{-8} ~ 10^{-7} Torr). This layer is then fully crystallized in vacuum at 500-550°C (crystallization temperature could be higher if STO is slightly off-stoichiometric), which results in SiO_2-free epitaxial STO on Si. The STO unit cell is rotated by 45º with respect to the conventional Si unit cell due to the lattice parameter of Si being $\sim\sqrt{2}$ times that of STO. Other perovskites, including BTO, which are epitaxially grown on the initial STO layer are expected to be crystallographically aligned with the STO template leading to an epitaxial relationship of (100)/(001) BTO // (100) Si and <010> BTO // <011> Si.

Once the initial template is crystallized, additional STO can be grown with two possible options. If the additional STO is again grown at low temperature (<300°C) with modest oxygen supply (mid 10^{-7} Torr) followed by annealing in vacuum to fully crystallize it, one would get a clean SiO_2-free interface between STO and Si. If instead one grows additional STO, treating the template as if it were a single crystal STO substrate, additional SiO_2 will be formed since oxygen has enough diffusivity in STO at the normal STO growth temperature of 500-550°C to reach Si. The resulting SiO_2 thickness in this case will increase as the total deposition time is prolonged. For STO layers less than 20 nm thick, this typically produces about 1-2 nm of SiO_2 interlayer between STO and Si.[35] Depending on whether or not the presence of this SiO_2 interlayer is critical for an application, the appropriate process for growing additional STO should be used. Note that despite the presence of this amorphous SiO_2 interlayer, the STO is still single crystal and in epitaxial registry to Si.

Given the findings of Hsu et al. that the STO buffer layer thickness affects the crystallographic orientation of MBE-grown films,[33] we also studied the effect of the STO buffer layer thickness on epitaxial sputtered BTO films. For this study, we grow 300 nm thick BTO films that are expected to be significantly relaxed to a-axis. Prior to BTO growth, STO templates were grown on Si with thicknesses of 2, 4, 6, and 8 nm. The RHEED patterns of the BTO films at the end of the 300-nm growth are shown in Fig. 2a-c. Fig. 2a shows BTO grown on 6 nm STO (the same pattern forms when grown on 8 nm STO) which exhibits an atomically flat, epitaxial surface. Fig. 2b is for BTO grown on 4 nm STO. The film is mostly epitaxial but shows signs of island formation and roughening. Fig. 2c is for BTO grown on 2 nm STO. While there are traces of epitaxy, the BTO has a substantial polycrystalline component as can be seen in the concentric rings in the RHEED pattern. It is clear that the 2 nm STO layer is disrupted by the relatively

harsh high temperature and high oxygen pressure conditions of the sputtering growth process. The 4 nm STO layer appears to be the threshold of where the STO remains stable against the sputtering deposition process, while at 6 nm, STO appears completely stable during the 300 nm BTO growth.

Importantly, we also need to determine how the BTO film is crystallographically oriented. For the most common electro-optic devices shown to date, we need a substantial fraction of BTO to be a-axis oriented (polar direction is in-plane). This is crucial for devices relying on the TE mode confined in a silicon or silicon nitride waveguide placed on the BTO layer. Fig. 2d-f shows x-ray diffraction scans taken from the 300 nm films grown on the different STO thicknesses on Si. The BTO grown on the 6- and 8-nm STO shows high quality films with about 55% a-axis average volume fraction. The BTO on the 4-nm film is of slightly worse quality but it is substantially a-axis oriented (90% volume fraction). The BTO grown on the 2-nm STO is also mostly a-axis oriented but the bigger problem is that it shows a strong 110 peak that is indicative of a large polycrystalline component, as expected from RHEED. While the volume fraction of a-axis is important, we also need the films to be dense and relatively smooth so for subsequent studies of thick film growth on Si, we will utilize STO buffer layers with 5-6 nm thickness.

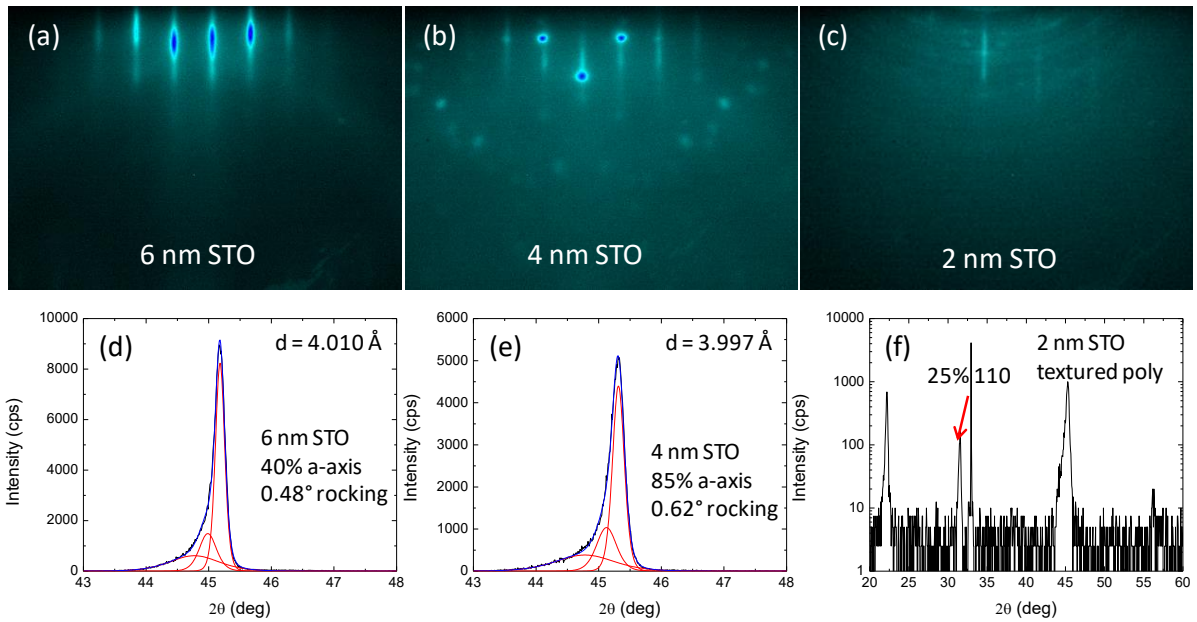

Figure 2. Effect of STO template layer thickness on quality of 300 nm BTO grown on top at 700°C. (a-c) RHEED images after growth of BTO on 6, 4, and 2 nm STO layers. An STO layer thickness of 4 nm appears to be the minimum one needs to obtain high quality epitaxial BTO. (d-f) X-ray diffraction of 300 nm BTO films grown on various thickness STO template layers. (d,e) The 6 nm STO layer gives higher quality BTO films (narrower rocking curve) compared to the 4 nm STO layer but the thinner STO appears to help with c-to-a axis relaxation resulting in more a-axis fraction for thinner STO. (f) The 2 nm film has a strong polycrystalline component, which is also seen in RHEED.

3.2. Crystallographic reorientation of thick BTO films

For this study, we utilize silicon-on-insulator wafers that are necessary for making functioning Si waveguides on top of the BTO. We use SOI wafers obtained from SOITEC where the device Si layer has been further thinned down from its original 220 nm thickness to 50-60 nm. The buried oxide layer is 2 μm thick. This substrate presents additional challenges with regards to thermal expansion mismatch since the BTO films are typically 5-10 times thicker than the

underlying device Si layer. Initial experiments revealed that the Si device layer cracks if the sample is cooled at more than 10°C/min. Plan view optical microscope and cross-section TEM imaging of fast-cooled samples reveal how cracks propagate down to the Si device layer (see Supporting Information, Fig. S7). Due to this issue, all films grown on SOI are cooled slowly (5-10°C/min) in the process gas until they reach 300°C after which the gas is removed. Cooling is continued slowly to room temperature. Note that samples grown on bulk Si are more tolerant to cracking and appear to be fine when cooled at 30-40°C/min.

Most reports of MBE-grown films seem to show onset of a-axis orientation when BTO thickness exceeds 25 nm and films are fully a-axis oriented when they get to ~120 nm thickness.[2,26-27] This appears to be different for sputtered films grown at the optimum growth conditions at high temperature and cooled slowly. Fig. 3a shows XRD 2θ–θ scans of the 200 region of BTO for various thickness films grown in a single high temperature step on thinned SOI substrates. Note that the data have been rescaled so that their maxima are approximately the same for easier comparison. There appears to be a highly strained c-axis component at a 2θ angle of 44.3-44.5°, which is then followed by a gradual relaxation towards relaxed c-axis at 44.8-44.9°, then through a "cubic" or mixed a/c phase at 45-45.2°, until a relaxed a-axis oriented phase appears at 45.3°. The relative amounts of each orientation component vary depending on the total BTO thickness. Films of 135 nm are completely c-axis oriented with significant residual compressive strain. This is unlike MBE-grown films which are already substantially a-axis oriented at this thickness. As the film is grown thicker, more of the mixed a/c and a-axis components contribute until at about 500 nm thickness when effectively >90% is a-axis oriented. The STO peak around 46.6° is also visible in these plots. The results of an orientation component analysis of the XRD curves for various thicknesses of BTO are shown in Fig. 3b. Typical full

range XRD 2θ–θ, rocking curve, and in-plane diffraction scans for a 500 nm film single-step-grown BTO film can be found in the Supporting Information, Fig. S8.

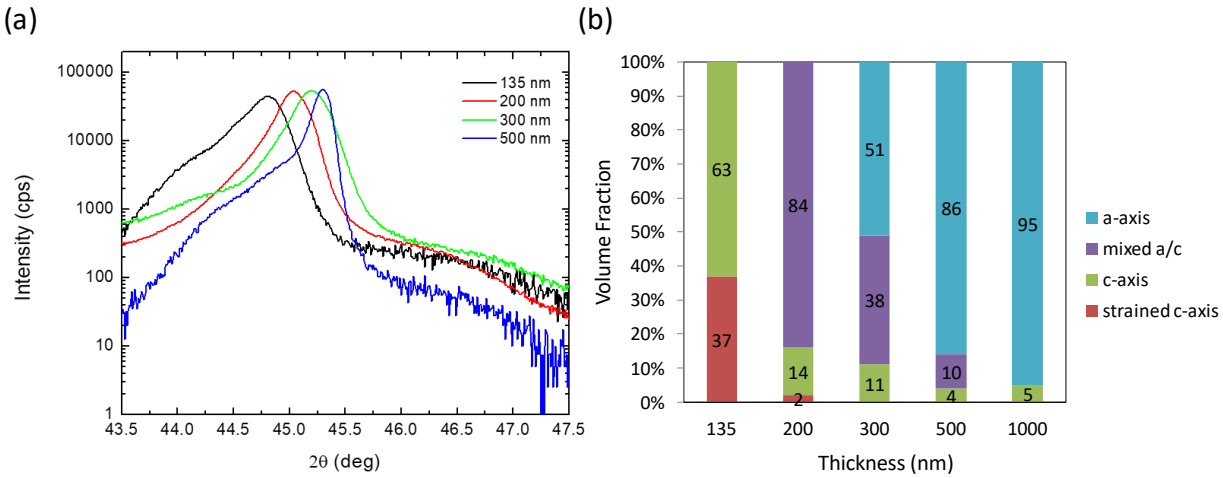

Figure 3. (a) Effect of total BTO film thickness on the out of plane lattice constant as measured by XRD. The data have been approximately normalized for easier visual comparison. One can see that the peak position shifts to higher angles (lower lattice constant) as the film thickness increases, consistent with the film transitioning from c-axis to a-axis orientation. Note that the 200 and 300 nm samples were measured without a monochromator. (b) Results of peak deconvolution of the BTO 002/200 Bragg reflection. The peaks have been binned into four categories and the relative amount (in %) of each category is plotted in the bar chart. The BTO film becomes majority a-axis oriented only at 300 nm thickness. The small amount of STO in each scan was excluded from the relative amounts listed. Note that no correction has been made to account for x-ray attenuation by the film thickness, which likely makes the true fraction of the buried c-axis layers to be slightly higher.

To better understand how the BTO film relaxes from c-orientation to a-orientation, high resolution ADF-STEM imaging was performed on a cross-section of a 500 nm sample. A low

magnification image showing the entire stack is shown in Fig. 4a whilst an atomically resolved image of the interface region with STO and Si is shown in Fig. 4b. One can see a high density of vertical white lines in Fig. 4a which are dislocations in the film and how the dislocation density decreases further away from the interface. The magnified ADF-STEM images (Fig. 4c) and corresponding atomic models (Fig. 4d) confirm the epitaxial relationship of <010> BTO/<010> STO on <011> Si. The observed microstructure is also consistent with a dense, highly crystalline film, which is what the Thornton zone model predicts for this growth condition (so-called Zone 2).[20-21]

To visualize how the lattice constant varies as a function of distance from the interface, we implemented geometric phase analysis (GPA) to determine variations in both the in-plane and out-of-plane lattice parameters. The GPA results are shown in Fig. 5. The left column shows the STEM images from which the GPA analysis was performed. The middle column is the GPA for the in-plane lattice parameter deviation using 3.99 Å as the central value. The right column is the GPA for the out of plane lattice parameter deviation. Brighter/warmer colors (red to yellow) signify the expansion of the lattice, while darker/colder colors (blue to black) represent compression of the lattice. Regardless of strain, the presence of dislocations gives a strong contrast difference to the areas where they exist, as indicated with small white arrows. The lattice parameters (both in-plane and out-of-plane) are calculated based on the strain values extracted from the GPA maps and plotted in Figure 6 as a function of distance following the black arrows in Figure 5. Because the presence of dislocations changes the local lattice parameters, regions that are dislocation-free were chosen for this analysis and defined by the black rectangles in Figure 5. The first region of analysis (bottom row) is close to the STO layer. The second region

(middle row) is close to half the BTO thickness. Finally, we sample the near surface region (top row).

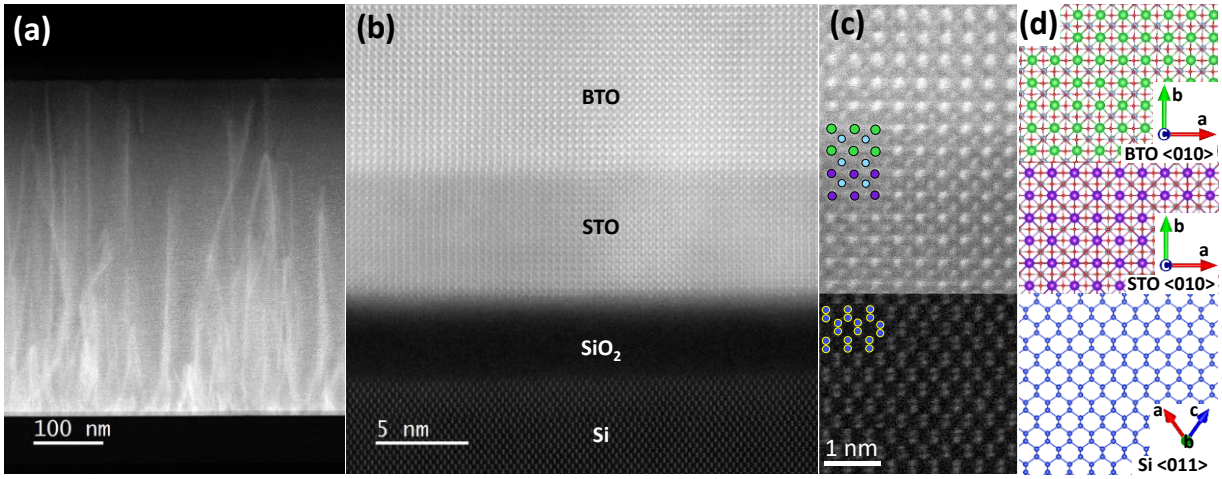

Figure 4. ADF-STEM images of the cross-section of a 500 nm BTO film grown at 700°C. (a) Low magnification image showing entire BTO layer. The vertical white lines are dislocations. (b) Atomic resolution image of the interface region of the same film. The BTO and STO are in epitaxial registry. There is a 3 nm amorphous SiO_2 interfacial layer that forms during the BTO deposition. (c,d) Magnified atomic resolution image matched with atomic model of BTO, STO, Si, showing the epitaxial relationship of (100) BTO // (100) Si and <010> BTO // <011> Si. Green, purple, cyan, red and blue circles represent Ba, Sr, Ti, O, and Si, respectively. The bottom portion of the STO layer and the amorphous SiO_2 layer have been cropped out for space reasons.

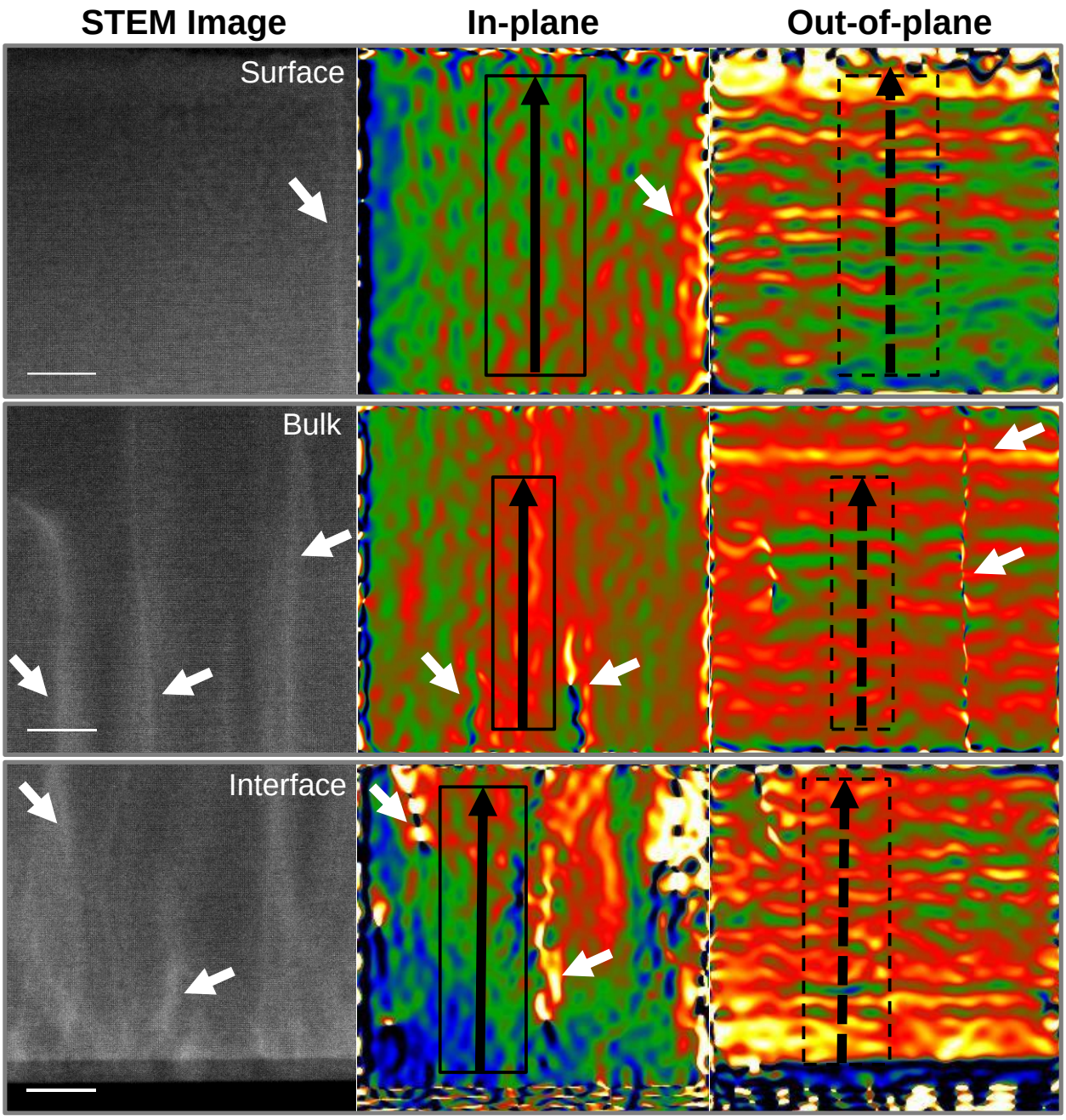
STEM Image
In-plane
Out-of-plane
Surface
Bulk
Interface

Figure 5. Geometric phase analysis of STEM images of three regions of the film. Top row corresponds to the near surface region; the middle row to the bulk region; and the bottom row to the near interface region. The STEM images used are shown in the left column; GPA results for the in-plane strain are shown in the middle column; and GPA results for the out of plane strain are shown in the right column. Dislocations are indicated by white arrows.

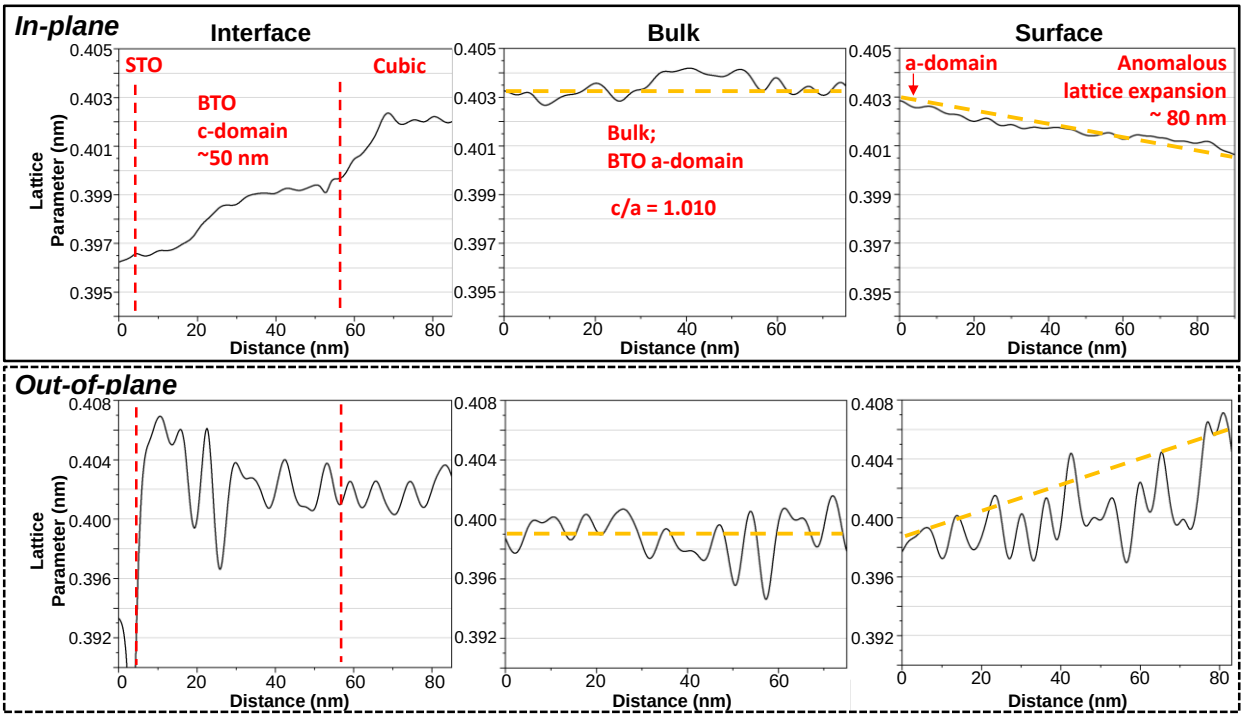

Figure 6. In-plane (top row) and out-of-plane (bottom row) lattice parameters of the BTO film as a function of relative layer position along the black solid/dashed arrows in Figure 5. The average of lattice parameter was obtained from the black solid/dashed boxed area in Figure 5. The left column is for the near interface region showing the transformation from strained c-axis to relaxed c-axis to a "cubic" orientation. The middle column is an area near half of the film thickness. This region is a-axis oriented with a tetragonality close to bulk BTO. The right column is for the near surface region. We can see the a-domain rapidly transitioning back through cubic and to a c-domain, as the in-plane lattice parameter decreases and out-of-plane lattice parameter increases. The c-domains right at the surface also exhibit an anomalous volume expansion in both its in-plane and out-of-plane lattice constants, compared to a bulk-like c-domain.

In order to better show the strain relaxation process in a 500 nm BTO film, we sampled several other regions to find transitions between different orientations and measured the mean in-plane and out of plane lattice constants by averaging around twenty lattice spacings using atomically resolved STEM images at each region. ADF-STEM images were carefully calibrated in both in-plane and out of plane directions using the bulk Si (220) lattice spacing under the BTO/STO layer before the measurements. The results of the lattice spacing analysis are summarized in Fig. 7 and Table 1 below.

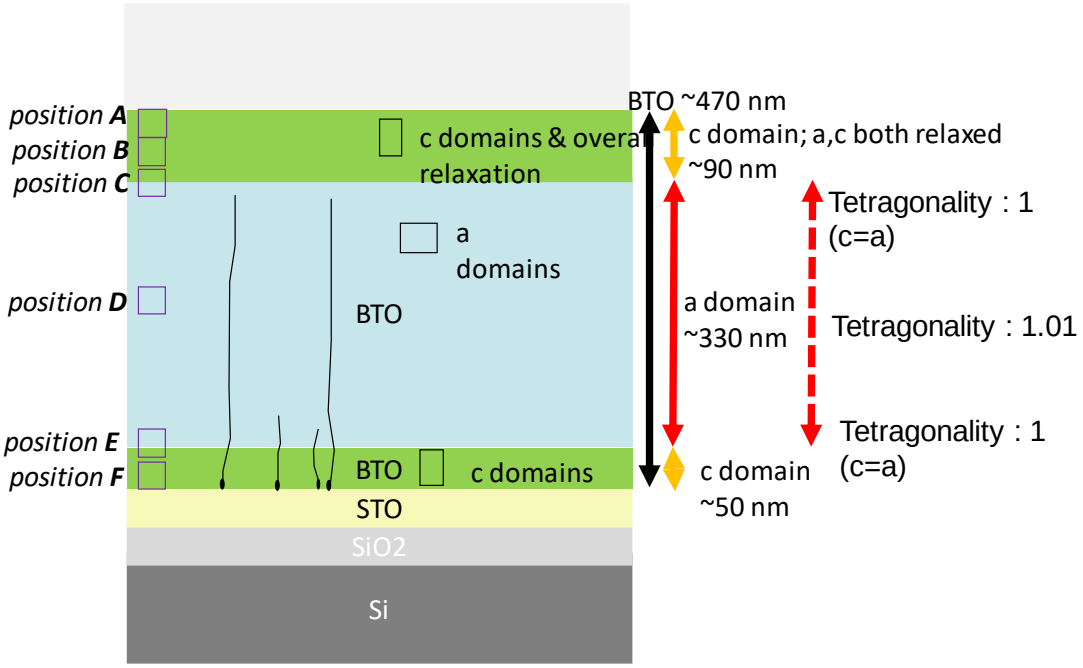

Figure 7. Analysis of mean lattice spacing taken from atomic resolution images at various positions across the film thickness (marked as positions A to F). A window of ten lattice spacings around each layer position is used for this analysis. There is a region that is c-axis oriented near the STO layer, a bulk like a-axis oriented region taking up about 70% of the film, and a near surface region that reverts to c-axis orientation with an anomalous expansion at the very surface.

Table 1: Quantification of the lattice constant averaging results of the various sampling positions indicated in Fig. 7.

Position		Horizontal	Vertical	c- or a-oriented?	Tetragonality (long/short)
A	the very surface	4.017	4.147	c [a/c both relaxed]	1.032361 (c/a>1)
B	surface	3.981	4.093	c	1.028204 (c/a>1)
C	~90nm from surface	4.027	4.012	a	1.003675 (c/a~1)
D	bulk	4.010	3.972	a	1.00967
D’	bulk	4.019	3.963	a	1.014165
D’’	bulk (80nm from the interface of BTO/STO)	4.004	3.937	a	1.01685
E	40nm from the interface	3.988	3.988	a=c=1	1(c/a=1)
F	interface	3.940	4.113	c	1.043739

As one expects, the BTO initially grows with c-axis orientation as it tries to match the smaller lattice of STO. This initial c-axis layer is partially strained to the STO with an in-plane spacing of 3.94 Å and out of plane spacing of 4.11 Å, which persists for about 15 nm before relaxing to the BTO bulk lattice constants, still c-axis oriented. The relaxed c-oriented film continues growing for another 30-40 nm at which point the in-plane and out of plane lattice constants become almost the same and the film becomes “cubic.” At 80 nm away from STO, there is the beginning of a gradual change to a-axis orientation as the out of plane spacing becomes smaller

than the in-plane spacing. This a-axis orientation persists for several hundred nm. At about 90 nm from the surface, the in-plane lattice constant begins to decrease gradually while the out of plane lattice constant simultaneously increases, with a fairly rapid increase near the surface. The in-plane lattice constant changes from 4.03 Å to 4.00 Å while the out of plane lattice constant changes from 3.99 Å to 4.06 Å. The c/a ratio becomes 1 at about 40 nm from the surface, after which the films become highly tetragonal with c-axis orientation. There is also an additional anomalous volume expansion right at the surface (~10 nm), with both ***a*** and ***c*** lattice parameters larger than their bulk values. It is unclear why the films re-transition to a volume-expanded c-axis orientation at the surface. The lattice expansion could be due to oxygen vacancies in the near surface region, which is known to expand the lattice of BTO.[43] It is possible that the highly energetic arriving species leads to preferential removal of O atoms that, in combination with the large electric field due to the sputtering gun, causes the surface to region to behave this way. More experiments are needed to fully understand the unusual surface behavior of the sputtered BTO film. Based on the STEM and GPA analysis, we find that for a 500 nm film, the middle ~350 nm is expected to be bulk-like a-axis oriented film with the rest consisting of strained c-axis, relaxed c-axis, cubic-like, and anomalous surface contributions. Note that this is somewhat less than what XRD analysis reveals, which indicates about 85% a-axis orientation rather than the 70% from TEM analysis.

The high-resolution STEM analysis also showed some of the common defects found in these thick sputtered BTO films on Si. Fig. 8a shows a low magnification image of a 500 nm BTO film. The bottom of the image is close to STO while the top is close to the surface. The STEM image shows that these sputtered films have almost no voids and have a high density very close to the surface, although a few surface cracks are found penetrating to about half the thickness of

the film as indicated by the red arrows. One can see a high density of white vertical lines, which are dislocations. The dislocations are more concentrated at the bottom and their density gradually decreases away from the interface. The dislocations are resolved at atomic resolution in Figs. 8b and 8c, which are atomic resolution STEM images taken along the [110] and [100] zone axis of BTO, respectively. If one follows along an atomic plane horizontally, the atomic species changes, e.g. a Ti plane becomes a Ba plane. By doing this for all planes, one can see that this transition forms a continuous boundary separating the left half of the image from the right half. These are known as anti-phase boundaries and can arise from stacking faults or from extra planes of BaO being inserted occasionally to correct for slight Ba excess, similar to what has been observed for STO.[44]

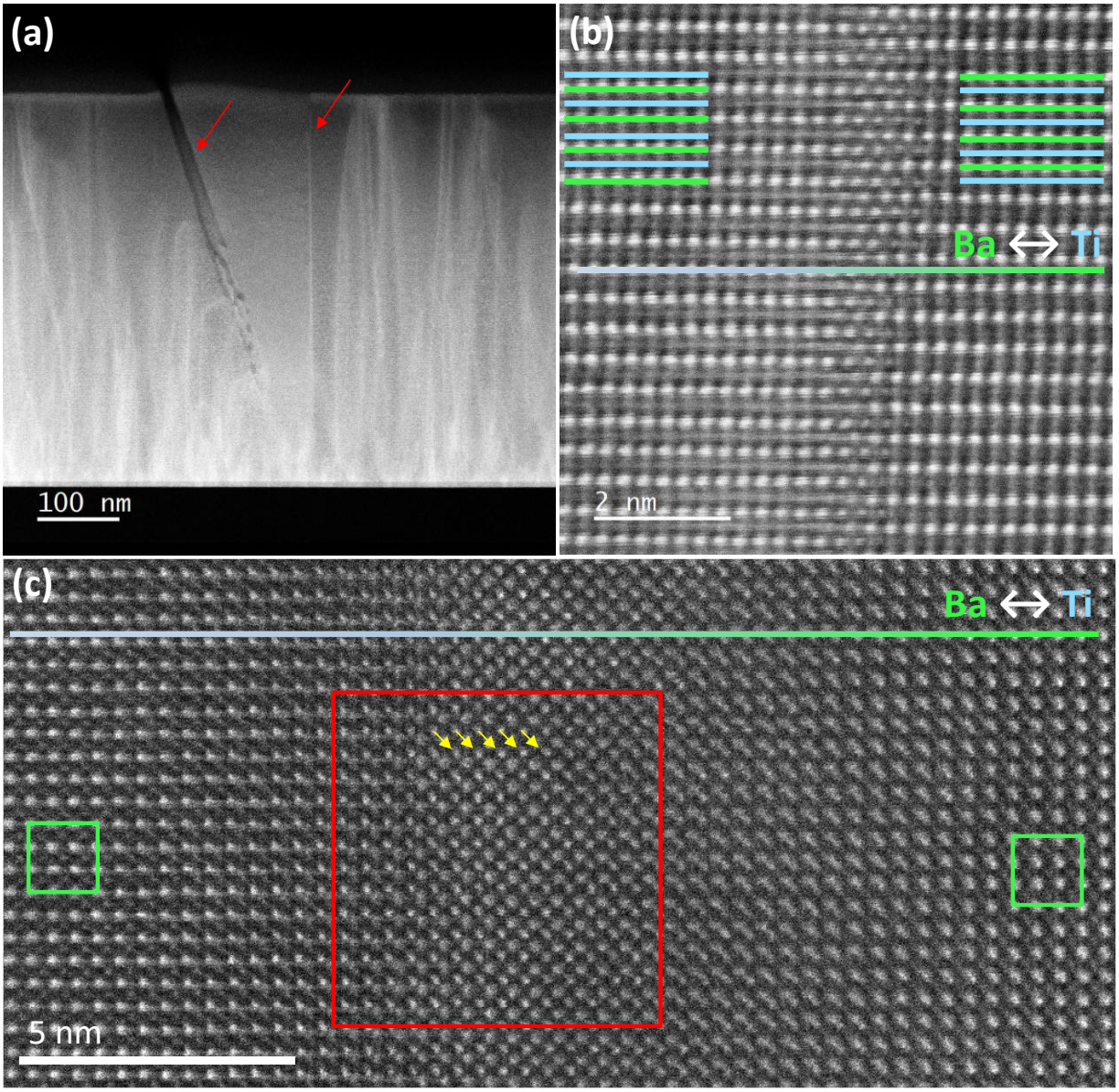
(a)
100 nm
(b)
Ba ↔ Ti
2 nm
(c)
Ba ↔ Ti
5 nm

Figure 8. Common defects found in the 500 nm BTO film. (a) The low magnification image shows a high density of white lines that gradually diminish away from the interface and towards the surface. These lines are dislocations. The image also shows a surface crack and a small misoriented crystallite at the surface (red arrows). (b, c) Atomic resolution image of an anti-phase boundary shown in the [110], and [100] zone axis of BTO, respectively. The TiO_2 layer becomes a BaO layer as one traces a particular atomic plane from left to right. The red-boxed area shows the transition of interchanging of Ba and Ti slabs.

3.3. Growth of 1-μm-thick films

While 500 nm films of excellent quality can be routinely grown, the growth of 1 μm films appears to be somewhat more complicated because of the extended growth time. We first attempted to grow 1 μm films in four segments of 250 nm each, with the sample being cooled down after each cycle. This resulted in a film having significant polycrystallinity and phase segregation (Ba_2TiO_4 and TiO_2), very poor 200 rocking curve (2.3° wide), surface cracking, and strong non-uniformity manifested in the color appearance of the surface. We then grew a 1 μm film using a single high temperature growth step at 700°C. The sample turned out mostly well but significant surface color non-uniformity likely due to uneven heating was still observable. Near the sample center, films were >95% a-axis, with a rocking curve width of 0.4° and with a good RHEED pattern. Comparison of the difference in RHEED and XRD patterns for the multi-step and single step growth is shown in Fig. 9.

With encouraging results for the 1-step process other than the temperature non-uniformity, two additional samples were grown with a lower and a higher deposition temperature. The lower deposition temperature (650°C) results in significant polycrystalline regions (>5%) with slightly

better uniformity. Raising the temperature seems to give very good results in terms of the BTO crystallinity and orientation but the visible non-uniformities become slightly worse. A photograph of the surface non-uniformities can be seen in the Supporting Information, Fig. S9. Obtaining uniform 1 μm-thick films will likely require a redesign of the sample holder to ensure uniform thermal gradients but the initial results for the single step growth are encouraging and allow for the growth of high quality epitaxial films at the micron level of thickness.

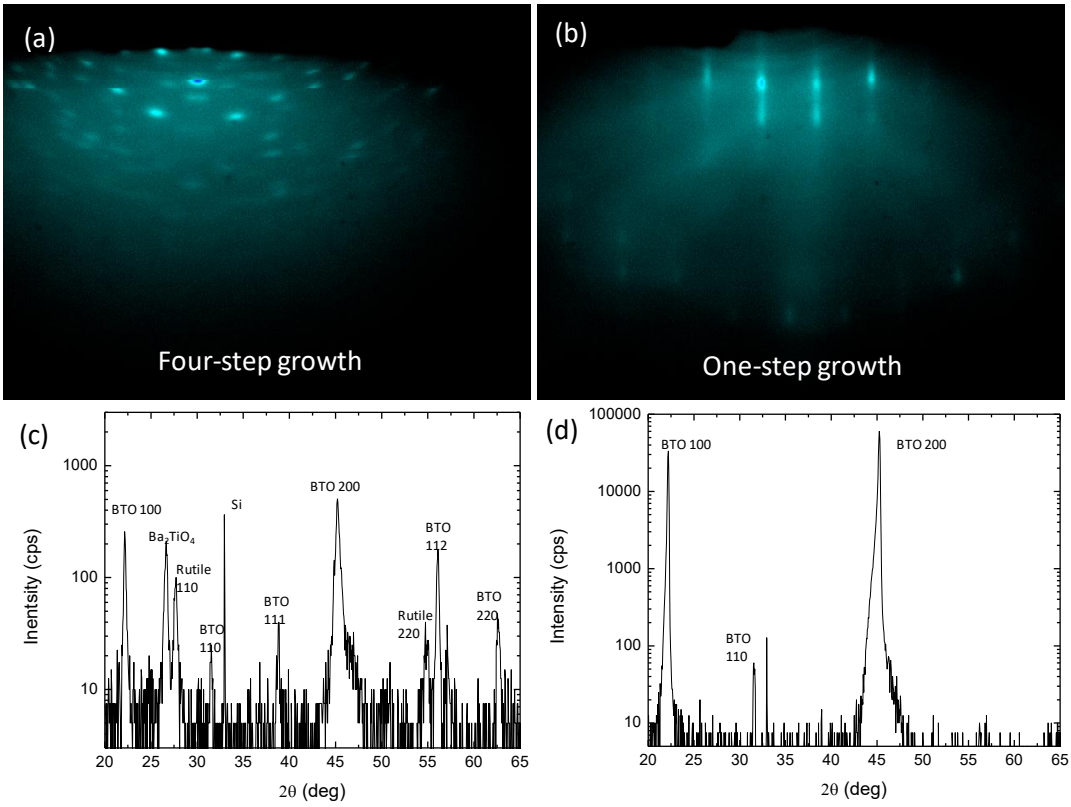

Figure 9. RHEED and XRD of 1 μm BTO films. (a) RHEED image of a 1 μm sample grown in four steps of 250 nm with a cool down to 200°C between each step (four-step growth). The film shows a cracked surface in optical microscopy (not shown) and the RHEED shows a rough island growth surface with a significant polycrystalline component. (b) RHEED image of a 1 μm sample grown in a single prolonged growth run (one-step growth). The RHEED shows a mostly epitaxial surface but with significant polycrystalline features as well. (c) XRD of the sample grown in four steps showing significant polycrystalline volume as well as phase segregation of TiO_2 and Ba_2TiO_4. (d) XRD of single step growth sample showing mostly a-axis oriented epitaxial film but with some amount of 110 orientation.

3.4. Maximizing a-axis fraction by recrystallization growth

In some cases, one might want a fully a-axis oriented epitaxial BTO film on Si with thickness down to 120 nm. As we have seen, it takes at least 300 nm for the sputtered BTO film to relax naturally so that majority of the film is a-oriented. For this reason, we have also looked at one possible way of obtaining a fully a-oriented film, following the initial reports of Abel et al.[45] and Wague et al.[27] If we grow an amorphous or barely crystalline film and crystallize it in a subsequent step, we should be able to get a seed layer of fully a-axis BTO. Additional growth of BTO on top of this seed layer is then expected to continue the a-orientation of the recrystallized seed layer. First, we studied the growth of BTO by sputtering at different substrate temperatures to determine what the crystallization temperature is. We grew 120 nm-thick BTO films at 500°C, 400°C, and 200°C (T/T_m of 0.40, 0.35, and 0.25, respectively). Films grown at 500 and 400°C are both crystalline but with strongly textured island growth while films grown at 200°C were amorphous, based on RHEED imaging after growth. The textured island growth is consistent

with the prediction of the Thornton structural zone model where one is expected to be in the so-called transition zone (Zone T) for these reduced growth temperatures.[20-21] All three 120-nm films were then subjected to a 30 min anneal at 750°C in a tube furnace with flowing oxygen. XRD analysis after annealing shows that the films were at least 98% a-axis oriented, with some residual c-orientation and 110 orientation present (typically a sign of random polycrystalline regions). It is surprising that BTO grown at 400°C was still crystalline before annealing, even though the surface was quite rough. Low temperature crystallization of BTO has been recently reported by Shin et al. in MBE-grown films.[46]

Given the ability to get almost fully a-oriented films at 120 nm thickness, we utilize this process to see if we can regrow epitaxial films on such recrystallized layers. We grow 60-80 nm-thick seed layers at 200 and 400°C and then subject them to an anneal in flowing oxygen at 750°C for 1 hour in a tube furnace. After confirming that the films are fully a-oriented by XRD, they are reloaded into the sputtering growth chamber and additional BTO is grown at 700°C to obtain a total thickness of 300-500 nm. XRD does indeed show that the entire film maintains its a-axis orientation although the island nature of the film surface remains and there is some amount of polycrystallinity that forms as well. Fig. 10a shows RHEED patterns for the 60 nm initial film grown at 400°C immediately after growth showing the island nature of the growth. Fig. 10b shows the XRD around the BTO 200 region confirming that the film is almost fully a-axis oriented after annealing. Fig. 10c shows the RHEED pattern for the same sample with additional BTO grown at 700°C to a total thickness of 500 nm. The island nature of the surface is retained. Fig. 10d shows a comparison of two 500-nm films, one grown using a single high temperature growth, and another using 2-step growth with a reduced crystallinity a-oriented 60-nm seed layer that was recrystallized, followed by a high temperature growth. One can see that

one indeed gets almost full a-axis orientation with the 2-step process at the cost of a rough surface.

We also prepared TEM cross-section samples of a sample grown using the two-step process to see what the microstructure of these films looked like. Both low and high magnification images of a selected region of such a film are shown in Fig. 11. As one can see, the near surface region is rough, marked by many gaps, some of which propagate down through the entire film. Fig. 11a shows that the initially poorly crystallized/amorphous seed layer of 60 nm is dense and does not have the pores but its surface is rough, as confirmed by RHEED. The additional thick BTO layer grown on top does not heal the roughness. In fact, the initial roughness appears to be the reason why gaps/pores form, as crystallites grow from all these various surfaces in slightly different directions. It can also be seen from the higher magnification image of Fig. 11b that there are several pockets of crystallites with different orientation, with most just misoriented 100-oriented grains, but some have totally different orientations (110 and 112 being the most common). The high degree of porosity, high roughness, and significant amount of misoriented grains makes films grown with a recrystallization step not suitable for electro-optic applications, even though this process can achieve almost a fully a-axis oriented film.

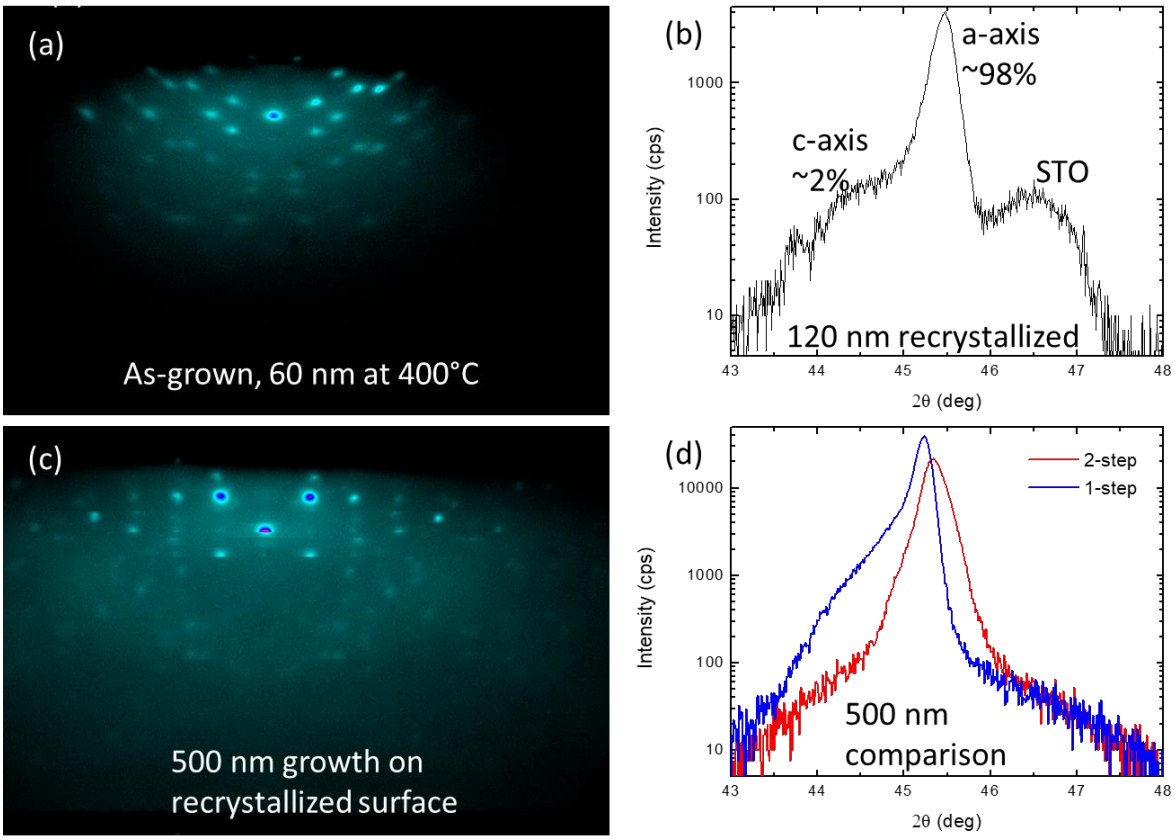

Figure 10. RHEED and XRD analysis of samples grown on recrystallized seed layers. (a) RHEED image of as-grown 120-nm BTO film grown at 400°C. The film is still crystalline but grows as oriented islands. (b) XRD of the BTO 200 region of the seed layer after annealing. One can see that almost the entire film is a-axis oriented even at a thickness of 120 nm. (c) RHEED image after additional BTO film grown on the recrystallized seed layer. The island nature of the growth surface is still present and some polycrystallinity is emerging. (d) Comparison of XRD scans of a 500 nm film grown in a single high temperature growth step (1-step) vs one grown on top of a recrystallized a-oriented seed layer (2-step). There is still about 10% c-axis orientation in the single-step film while there is about 0.1% in the two-step process.

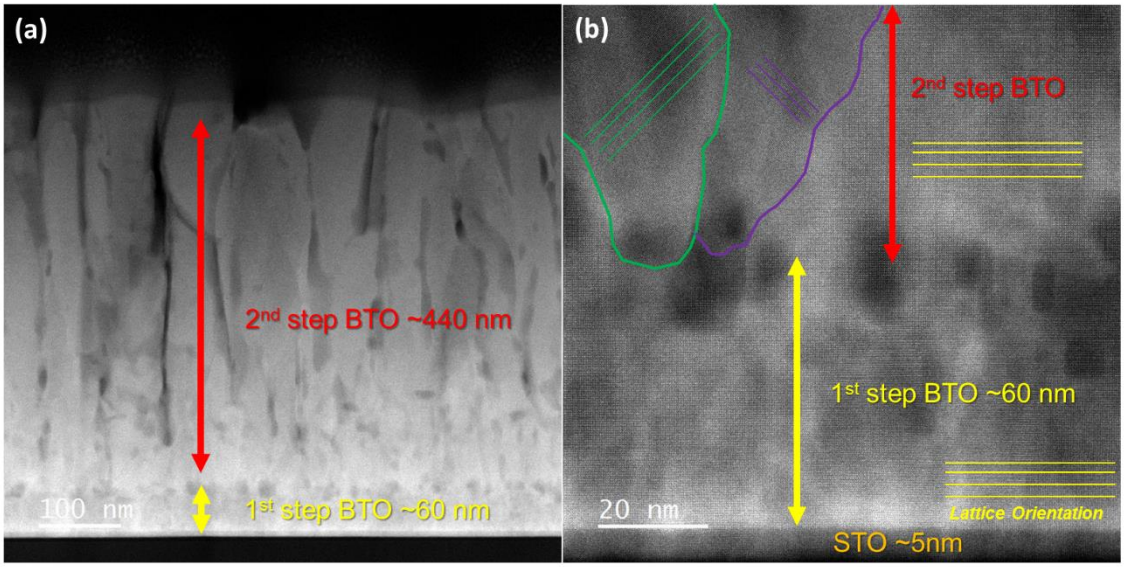

Figure 11. Cross-section STEM images of a 500 nm film grown on a recrystallized a-axis seed layer. (a) Low magnification image showing that the 60 nm BTO seed layer is dense and pore-free, while the subsequent BTO grains grown on top of the BTO seed layer has a significant amount of pores and a rough surface, which is only worsened by the subsequent growth. (b) High magnification image showing BTO multi-grains that are misoriented from each other on top of the single crystal BTO seed layer, epitaxial to the STO layer below.

3.5. Electro-optic measurements

Electro-optic measurements have been performed previously on BTO films grown using various methods.[14] The expectation is that high quality films that are relatively pore free, have high tetragonality, and have long range epitaxial order will give a larger Pockels coefficient.[7] Free space Pockels measurements were performed using the same setup used in Reynaud et al.[38] on a 300 nm sputtered film grown in a single growth step at 700°C, which showed a 55% effective a-axis orientation. The electro-optic response is defined as the change in the index of refraction as a function of applied electric field and the Pockels response is given as

$$n_{ij}(E) = n_{ij}(0) - \frac{1}{2} n_{ij}(0) r_{ijk} E_k \quad (1)$$

where index k specifies the orientation of the applied electric field. A schematic of the measurement is shown in Fig. 12a. From prior work,[2] it is known that for tetragonal BTO, the r_{42}/r_{51} Pockels coefficient is the dominant coefficient. Therefore, we restrict ourselves to measurements of devices that couple strongly the applied electric field to the r_{42} coefficient, which are pads that are oriented at a 45° angle with respect to the polar axis of the film, as shown in Fig. 12b. Briefly, the measurement involves measuring the direct power P incident on the photodetector, along with the modulated power ΔP. The equations for these are shown as an inset in Fig. 12c, which shows the data fitting from which the Pockels coefficient is extracted. By fitting the data as $\Delta P/P \ vs. \theta_a$, we can extract the coefficient $\delta/2$, which is the rotation of the light after passing through the quarter wave plate due the phase shift from the Pockels effect. To extract the coefficient, we use[38]

$$r_{eff} = \frac{(2\,(\delta/2))\lambda_0}{\pi n^3 E_{a.c.} l \upsilon} \quad (2)$$

where λ_0 = 1550 nm, $n = 2.21$,[7] $E_{a.c.}$ is the rms electric field in the film, which is 1.77×10^5 V/m (we assume that the field approximately follows $E = V/d$ for a film of this thickness), l is the thickness of active a-axis BTO (~165 nm) and υ is a geometrical constant related to how much of the film will contribute to the response seen. For tetragonal BTO on a 45° pad with respect to the crystalline axes, this constant is 1.[2] To confirm that the results seen do not originate from the Kerr effect[2] (a change in the index of refraction with respect to the applied field squared) measurements were carried out by testing the change of the modulation of the signal (ΔP)) for a specific analyzer angle value with respect to changing the applied AC field, with the DC field held constant. This was normalized by the DC power *P*. The result of this is shown in Fig. 12d. For the Pockels effect, the modulation vs amplitude of the applied AC field

should be linear while for the Kerr effect is should be quadratic. Clearly a linear dependence is seen confirming that the modulation shown does not originate from the Kerr effect.

To give further evidence that the modulated response is the Pockels response, a measurement is performed where the polarization angle θ_i of the incident light is varied (by rotating the half-wave plate) while keeping the pad angle ϕ_E held constant at 45°. The result of this measurement is shown in Fig. 12e. To assess the average response of the entire BTO sample, multiple pads and different peaks and minima were measured, with the peaks being measured multiple times per pad. This yields an average effective Pockels coefficient of 131 $\pm$ 36 pm/V, where the error shown represents one standard deviation. The maximum response seen is 183 pm/V, assuming only the a-oriented volume fraction of the film responds to the modulation. Points where the signal was reduced to noise were also seen at 50° and 140°.[47] This is an additional indicator that what is being seen here is in fact the Pockels response.[38] In addition to the errors discussed in Reynaud et al.,[38] there is also noticeable variation due to contact resistance between the tungsten contact pads on the sample and the probes with which the voltage is applied. It is also possible that the local BTO quality (dislocation density) and domain population varies between different tungsten contacts, and that the amount of time the film has been poled in a specific orientation could also affect the measurement.

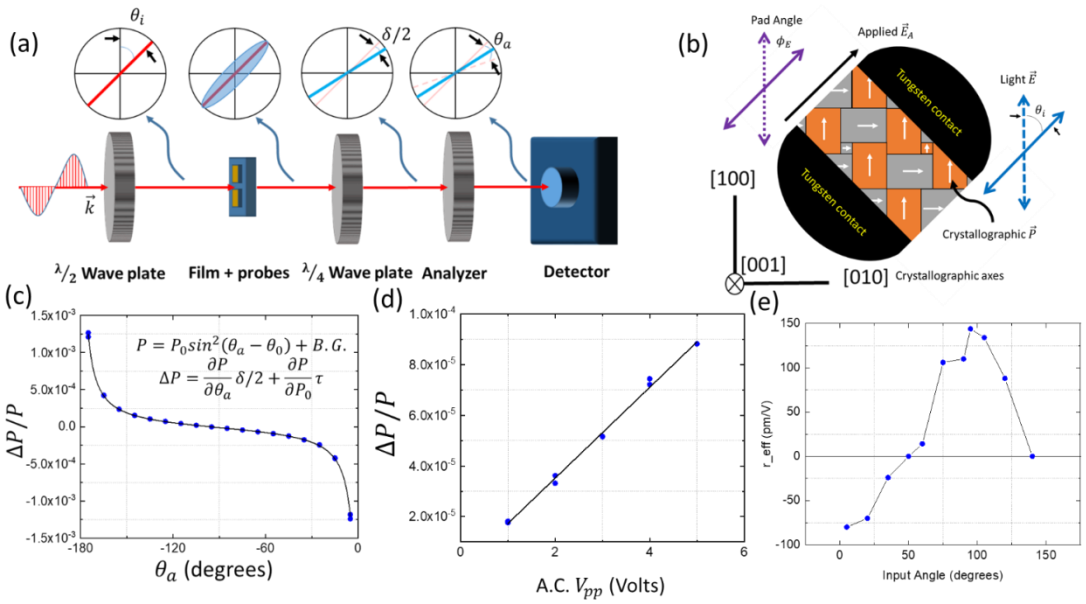

Figure 12. (a) Schematic showing the beam path for the free space transmission electro-optic measurement. (b) Example tungsten contact pad with BTO in between, showing a 45° angle between the BTO polar axis and the applied E field. (c) Example fitting of data from which the Pockels coefficient is extracted. (d) Measurement of dP/P vs the applied AC field showing that the response is linear with respect to the field. (e) r_{eff} vs input angle showing the dependence on the input angle for the Pockels response.

To confirm the Pockels coefficient obtained from the transmission measurement, MZM devices were fabricated on the sputtered BTO films (Fig. 13a). The device is designed to be placed at a certain angle so that the in-plane electrical field induced by the device electrodes is 45 degrees with respect to the BTO in-plane domains, thus leveraging both domain orientations during the modulation. Prior to the measurement, the MZM was first poled using a field of 165 kV/cm to orient the BTO in-plane domains. Light with wavelengths centered around 1550 nm is sent through the waveguide via a grating coupler. When a voltage is applied to the gold contacts, we observe reliable voltage-induced phase shifting of the optical signal (Fig. 13b). The observed

effective index change is 1.8393×10^{-4} at 1 V DC voltage yielding an effective Pockels coefficient of 157.5 pm/V. The $V_{\pi}L$ product for the device is calculated to be 0.421 V-cm, which is similar to what Abel et al. reported.[48]

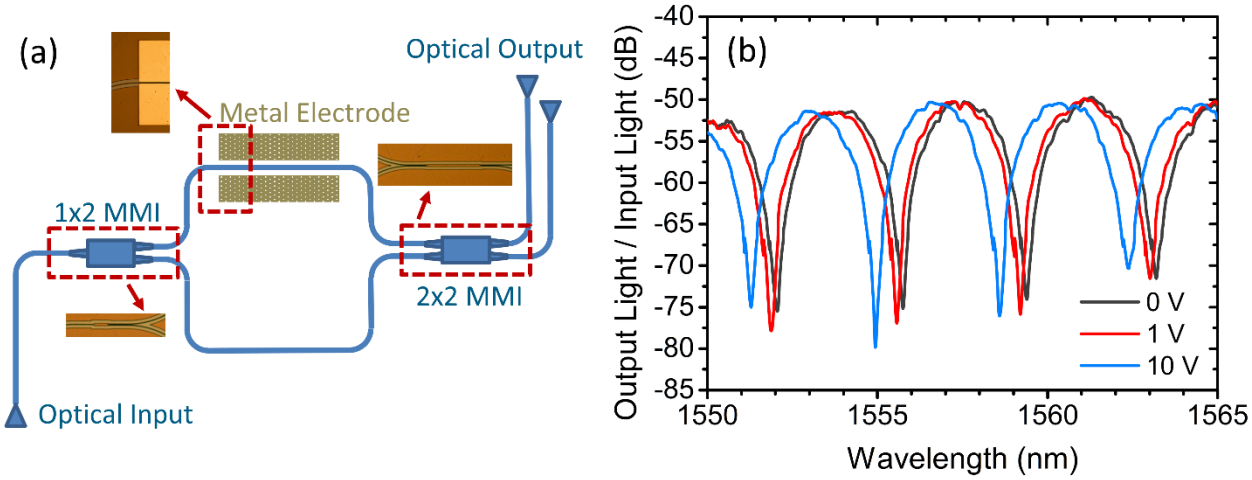

Figure 13. (a) Schematic diagram of the MZM, with optical microscope images showing 1x2 MMI, 2x2 MMI and a section of active region with electrodes. (b) The MZM modulation response under various DC voltages.

The extracted Pockels coefficient values of 131 pm/V and 157 pm/V obtained from the transmission and MZM measurements are significantly lower than the record for an MBE-grown thick film but is still much better than bulk $LiNbO_3$ and is an improvement over prior reports of sputtered BTO grown epitaxially on Si using an MBE-grown buffer layer.[7,49] A column graph is shown in Fig. 14 comparing the response in the sputtered films here to what has been seen in the literature. It should be noted that this is the first work in which rigorous investigation has been carried out to determine the a-axis fraction of BTO in the film. It can be seen that the values measured for the sputtered films are on par with most MBE-grown BTO films on Si.

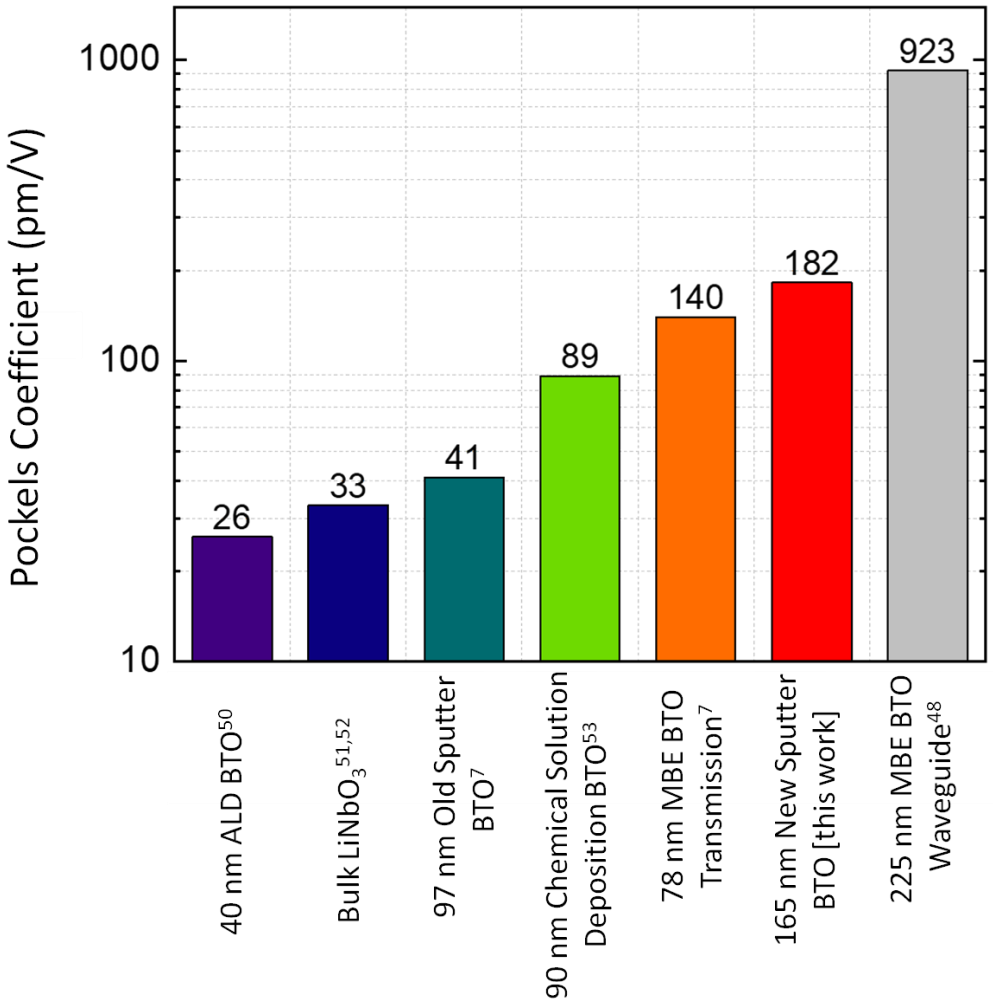

Figure 14. Graph showing the Pockels coefficient of BTO thin films integrated on Si using various growth techniques along with a comparative value for bulk $LiNbO_3$. Except for the waveguide measurement, all values for BTO films were measured in a free space transmission geometry and are listed as the effective Pockels response. The listed coefficient for the waveguide measurement is the largest tensor component, extracted after accounting for domain structure and device geometry, as reported in Abel at al.[48]

4. Conclusions

Highly crystalline, epitaxial $BaTiO_3$ films with a-axis orientation and thickness >300 nm were grown by off-axis RF magnetron sputtering on silicon-on-insulator substrates for use in waveguide geometry electro-optic applications. The films are structurally of similar quality as those grown by molecular beam epitaxy but can be grown ten times faster, allowing for a path for manufacturability of such thick films. Transmission electro-optic measurements of the Pockels coefficient yields an average value of 131 pm/V, which is over four times the value for bulk $LiNbO_3$, the current industry standard, and reaching as high as 183 pm/V. Measurement of a Mach-Zehnder modulator fabricated on such films confirms electro-optic modulation of the phase with an equivalent Pockels coefficient consistent with the transmission data (157 pm/V) and a $V_\pi L$ value of 0.421 V-cm. Such thick epitaxial films integrated on Si can enable reductions in both power and size requirements for electro-optic modulators allowing them to be incorporated directly on-chip.

Corresponding Author

*demkov@physics.utexas.edu

Supporting Information

Document describing auxiliary measurements performed on the samples are available. These include x-ray reflectivity, x-ray photoelectron spectroscopy, sputtering gun distance optimization, typical XRD data, and photographs of sample surfaces.

Author Contributions

The manuscript was written through contributions of all authors. ABP and AAD designed the overall project and coordinated the writing. ABP performed growth, x-ray diffraction, and x-ray photoelectron spectroscopy. HP and JHW performed the TEM analysis. ABP and WG did the STO thickness dependence study. ABP and IB performed the sputter gun position study. MR performed and analyzed the transmission Pockels effect measurements. WC, JDR, VJ, and GM performed the SOI wafer thinning and electro-optic modulator fabrication and measurement. All authors have given approval to the final version of the manuscript.

Funding Sources

This work was supported by the Air Force Office of Scientific Research under Award No FA9550-18-1-0053.

ACKNOWLEDGMENT

The authors are very grateful to Raluca Gearba for preparing the TEM cross-section samples.

REFERENCES

(1) Wessels, B. W. Ferroelectric Epitaxial Thin Films for Integrated Optics. Annu. Rev. Mater. Res., 2007, 37 (1), 659–679.

(2) Abel, S.; Stöferle, T.; Marchiori, C.; Rossel, C.; Rossell, M. D.; Erni, R.; Caimi, D.; Sousa, M.; Chelnokov, A.; Offrein, B. J.; Fompeyrine, J. A Strong Electro-Optically Active Lead-Free Ferroelectric Integrated on Silicon. Nat Commun., 2013, 4 (1), 1671.

(3) Kumah, D. P.; Ngai, J. H.; Kornblum, L. Epitaxial Oxides on Semiconductors: From Fundamentals to New Devices. Adv. Funct. Mater., 2019, 30 (18), 1901597.

(4) Eltes, F.; Mai, C.; Caimi, D.; Kroh, M.; Popoff, Y.; Winzer, G.; Petousi, D.; Lischke, S.; Ortmann, J. E.; Czornomaz, L.; Zimmerman, L.; Fompeyrine, J.; Abel, S. A $BaTiO_3$-Based Electro-Optic Pockels Modulator Monolithically Integrated on an Advanced Silicon Photonics Platform. J. Lightwave Technol., 2019, 37 (5), 1456–1462.

(5) Abel, S.; Fompeyrine, J. "Electro-optically active oxides on silicon for photonics," in *Thin Films on Silicon*, edited by V. Narayanan, M. Frank, and A. A. Demkov (World Scientific, Singapore, 2016), p. 455.

(6) Qiu, J. H.; Ding, J. N.; Yuan, N. Y.; Wang, X. Q.; Zhou, Y. Film Thickness Dependence of Electro-Optic Effect in Epitaxial $BaTiO_3$ Thin Films. Solid State Communications, 2011, 151 (19), 1344–1348.

(7) Kormondy, K. J.; Popoff, Y.; Sousa, M.; Eltes, F.; Caimi, D.; Rossell, M. D.; Fiebig, M.; Hoffmann, P.; Marchiori, C.; Reinke, M.; Trassin, M.; Demkov, A. A.; Fompeyrine, J.; Abel, S. Microstructure and Ferroelectricity of $BaTiO_3$ Thin Films on Si for Integrated Photonics. Nanotechnology, 2017, 28 (7), 075706.

(8) Schwartzkopf, M.; Hinz, A.; Polonskyi, O.; Strunskus, T.; Löhrer, F. C.; Körstgens, V.; Müller-Buschbaum, P.; Faupel, F.; Roth, S. V. Role of Sputter Deposition Rate in Tailoring Nanogranular Gold Structures on Polymer Surfaces. ACS Appl. Mater. Interfaces 2017, 9 (6), 5629–5637.

(9) Towner, D. J.; Ni, J.; Marks, T. J.; Wessels, B. W. Effects of Two-Stage Deposition on the Structure and Properties of Heteroepitaxial $BaTiO_3$ Thin Films. Journal of Crystal Growth, 2003, 255 (1–2), 107–113.

(10) Towner, D. J.; Lansford, T. J.; Wessels, B. W. Three Dimensional Domain Structure in Epitaxial Barium Titanate Thin Films. J. Electroceram., 2004, 13 (1–3), 89–93.

(11) Wooten, E. L.; Kissa, K. M.; Yi-Yan, A.; Murphy, E. J.; Lafaw, D. A.; Hallemeier, P. F.; Maack, D.; Attanasio, D. V.; Fritz, D. J.; McBrien, G. J.; Bossi, D. E. A Review of Lithium Niobate Modulators for Fiber-Optic Communications Systems. IEEE J. Select. Topics Quantum Electron., 2000, 6 (1), 69–82.

(12) Jianheng Li; Zhifu Liu; Yongming Tu; Seng-Tiong Ho; Il Woong Jung; Ocola, L. E.; Wessels, B. W. Photonic Crystal Waveguide Electro-Optic Modulator with a Wide Bandwidth. J. Lightwave Technol., 2013, 31 (10), 1601–1607.

(13) Xiong, C.; Pernice, W. H. P.; Ngai, J. H.; Reiner, J. W.; Kumah, D.; Walker, F. J.; Ahn, C. H.; Tang, H. X. Active Silicon Integrated Nanophotonics: Ferroelectric $BaTiO_3$ Devices. Nano Lett., 2014, 14 (3), 1419–1425.

(14) Guo, W.; Posadas, A. B.; Demkov, A. A. Epitaxial Integration of $BaTiO_3$ on Si for Electro-Optic Applications. Journal of Vacuum Science & Technology A, 2021, 39 (3), 030804.

(15) Mazet, L.; Yang, S. M.; Kalinin, S. V.; Schamm-Chardon, S.; Dubourdieu, C. A Review of Molecular Beam Epitaxy of Ferroelectric $BaTiO_3$ films on Si, Ge and GaAs Substrates and Their Applications. Science and Technology of Advanced Materials, 2015, 16 (3), 036005.

(16) Kester, D. J.; Messier, R. Micro-Effects of Resputtering Due to Negative Ion Bombardment of Growing Thin Films. J. Mater. Res., 1993, 8 (8), 1938–1957.

(17) Pratt, I. H.; Firestone, S. Fabrication of RF-Sputtered Barium Titanate Thin Films. Journal of Vacuum Science and Technology, 1971, 8 (1), 256–260.

(18) Lee, N.-Y.; Sekine, T.; Ito, Y.; Uchino, K. Deposition Profile of RF-Magnetron-Sputtered $BaTiO_3$ Thin Films. Jpn. J. Appl. Phys., 1994, 33 (Part 1, No. 3A), 1484–1488.

(19) Lyu, J.; Estandía, S.; Gazquez, J.; Chisholm, M. F.; Fina, I.; Dix, N.; Fontcuberta, J.; Sánchez, F. Control of Polar Orientation and Lattice Strain in Epitaxial $BaTiO_3$ Films on Silicon. ACS Appl. Mater. Interfaces, 2018, 10 (30), 25529–25535.

(20) Thornton, J. A. High Rate Thick Film Growth. Annu. Rev. Mater. Sci. 1977, 7 (1), 239–260.

(21) Anders, A. A Structure Zone Diagram Including Plasma-Based Deposition and Ion Etching. Thin Solid Films 2010, 518 (15), 4087–4090.

(22) Vargas, F. A.; Nouar, R.; Said Bacar, Z.; Higuera, B.; Porter, R.; Sarkissian, A.; Thomas, R.; Ruediger, A. On-Axis Radio Frequency Magnetron Sputtering of Stoichiometric $BaTiO_3$ Target: Localized Re-Sputtering and Substrate Etching during Thin Film Growth. Thin Solid Films, 2015, 596, 77–82.

(23) Buchal, Ch.; Beckers, L.; Eckau, A.; Schubert, J.; Zander, W. Epitaxial $BaTiO_3$ Thin Films on MgO. Materials Science and Engineering: B, 1998, 56 (2–3), 234–238.

(24) Srikant, V.; Tarsa, E. J.; Clarke, D. R.; Speck, J. S. Crystallographic Orientation of Epitaxial $BaTiO_3$ films: The Role of Thermal-expansion Mismatch with the Substrate. Journal of Applied Physics, 1995, 77 (4), 1517–1522.

(25) Li, W.; Landis, C. M.; Demkov, A. A. Polarization and Crystallographic Domain Morphology in Si-Integrated Epitaxial $BaTiO_3$ films. Manuscript in preparation.

(26) Dubourdieu, C.; Bruley, J.; Arruda, T. M.; Posadas, A.; Jordan-Sweet, J.; Frank, M. M.; Cartier, E.; Frank, D. J.; Kalinin, S. V.; Demkov, A. A.; Narayanan, V. Switching of Ferroelectric Polarization in Epitaxial $BaTiO_3$ Films on Silicon without a Conducting Bottom Electrode. Nature Nanotech., 2013, 8 (10), 748–754.

(27) Wagué, B.; Brubach, J.- B.; Niu, G.; Dong, G.; Dai, L.; Roy, P.; Saint-Girons, G.; Rojo-Romeo, P.; Robach, Y.; Vilquin, B. Structural Studies of Epitaxial $BaTiO_3$ Thin Film on Silicon. Thin Solid Films, 2020, 693, 137636.

(28) Jimi, M.; Ohnishi, T.; Terai, K.; Kawasaki, M.; Lippmaa, M. Strain-Driven Domain Structure Control and Ferroelectric Properties of $BaTiO_3$ Thin Films. Thin Solid Films, 2005, 486 (1–2), 158–161.

(29) Zhang, W.; Yuan, M.; Wang, X.; Pan, W.; Wang, C.-M.; Ouyang, J. Design and Preparation of Stress-Free Epitaxial $BaTiO_3$ polydomain Films by RF Magnetron Sputtering. Science and Technology of Advanced Materials, 2012, 13 (3), 035006.

(30) Scigaj, M.; Chao, C. H.; Gázquez, J.; Fina, I.; Moalla, R.; Saint-Girons, G.; Chisholm, M. F.; Herranz, G.; Fontcuberta, J.; Bachelet, R.; Sanchez, F. High Ferroelectric Polarization in c-Oriented $BaTiO_3$ Epitaxial Thin Films on $SrTiO_3$/Si(001). Appl. Phys. Lett., 2016, 109 (12), 122903.

(31) Qiao, L.; Bi, X. fang. Microstructural Orientation, Strain State and Diffusive Phase Transition of Pure Argon Sputtered $BaTiO_3$ film. J. Phys. D: Appl. Phys., 2009, 42 (17), 175508.

(32) Kawai, M.; Kan, D.; Isojima, S.; Kurata, H.; Isoda, S.; Shimakawa, Y.; Kimura, S.; Sakata, O. Critical Thickness Control by Deposition Rate for Epitaxial $BaTiO_3$ Thin Films Grown on $SrTiO_3$(001). Journal of Applied Physics, 2007, 102 (11), 114311.

(33) Hsu, M.-H. M.; Van Thourhout, D.; Pantouvaki, M.; Meersschaut, J.; Conard, T.; Richard, O.; Bender, H.; Favia, P.; Vila, M.; Cid, R.; Rubio-Zuazo, J.; Castro, G. R.; Van Campenhout, J.; Absil, P.; Merckling, C. Controlled Orientation of Molecular-Beam-Epitaxial $BaTiO_3$ on Si(001) Using Thickness Engineering of $BaTiO_3$ and $SrTiO_3$ buffer Layers. Appl. Phys. Express, 2017, 10 (6), 065501.

(34) Merckling, C.; Korytov, M.; Celano, U.; Hsu, M.-H. M.; Neumayer, S. M.; Jesse, S.; de Gendt, S. Epitaxial Growth and Strain Relaxation Studies of $BaTiO_3$ and $BaTiO_3$/$SrTiO_3$ Superlattices Grown by MBE on $SrTiO_3$-Buffered Si(001) Substrate. Journal of Vacuum Science & Technology A, 2019, 37 (2), 021510.

(35) Choi, M.; Posadas, A.; Dargis, R.; Shih, C.-K.; Demkov, A. A.; Triyoso, D. H.; David Theodore, N.; Dubourdieu, C.; Bruley, J.; Jordan-Sweet, J. Strain Relaxation in Single Crystal $SrTiO_3$ Grown on Si (001) by Molecular Beam Epitaxy. Journal of Applied Physics, 2012, 111 (6), 064112.

(36) Humboldt University – Structure Research and Electron Microscopy Group, *Useful plugins and scripts for Digital Micrograph*, https://www.physics.hu-berlin.de/en/sem/software/software_frwrtools (Accessed, 28 July 2021)

(37) Hÿtch, M. J.; Putaux, J. -L.; Pénisson, J.-M. Measurement of the Displacement Field of Dislocations to 0.03 Å by Electron Microscopy. Nature, 2003, 423 (6937), 270–273.

(38) Reynaud, M.; Chen, P.-Y.; Li, W.; Paoletta, T.; Kwon, S.; Lee, D. H.; Beskin, I.; Posadas, A. B.; Kim, M. J.; Landis, C. M.; Lai, K.; Ekerdt, J. G.; Demkov, A. A. Electro-Optic Response in Epitaxially Stabilized Orthorhombic mm2 $BaTiO_3$. Phys. Rev. Materials, 2021, 5 (3), 035201.

(39) Reiner, J. W.; Kolpak, A. M.; Segal, Y.; Garrity, K. F.; Ismail-Beigi, S.; Ahn, C. H.; Walker, F. J. Crystalline Oxides on Silicon. Adv. Mater., 2010, 22 (26–27), 2919–2938.

(40) McKee, R. A.; Walker, F. J.; Chisholm, M. F. Crystalline Oxides on Silicon: The First Five Monolayers. Phys. Rev. Lett., 1998, 81 (14), 3014–3017.

(41) Demkov, A. A.; Posadas, A. B. *Integration of Functional Oxides on Semiconductors,* (Springer-Verlag, New York, 2014)

(42) Fredrickson, K. D.; Seo, H.; Demkov, A. A. Mechanism of Oxidation Protection of the Si(001) Surface by Sub-Monolayer Sr Template. Journal of Applied Physics, 2016, 120 (6), 065301.

(43) Zhao, T.; Chen, F.; Lu, H.; Yang, G.; Chen, Z. Thickness and Oxygen Pressure Dependent Structural Characteristics of $BaTiO_3$ Thin Films Grown by Laser Molecular Beam Epitaxy. Journal of Applied Physics 2000, 87 (10), 7442–7447.

(44) Wu, H.; Aoki, T.; Posadas, A. B.; Demkov, A. A.; Smith, D. J. Anti-Phase Boundaries at the $SrTiO_3$/Si(001) Interface Studied Using Aberration-Corrected Scanning Transmission Electron Microscopy. Appl. Phys. Lett., 2016, 108 (9), 091605.

(45) Abel, S.; Sousa, M.; Rossel, C.; Caimi, D.; Rossell, M. D.; Erni, R.; Fompeyrine, J.; Marchiori, C. Controlling Tetragonality and Crystalline Orientation in $BaTiO_3$ Nano-Layers Grown on Si. Nanotechnology, 2013, 24 (28), 285701.

(46) Shin, Y. J.; Jiang, J.; Jia, Y.; Walker, F. J.; Ahn, C. H. Low Temperature Growth of Epitaxial Ferroelectric $BaTiO_3$. APL Materials, 2021, 9 (4), 041104.

(47) During measurements, the sample was unmounted and remounted. This changed the input angle θ_i which yielded noise in the lock-in amplifier signal. The peaks were shifted slightly (by about ~4-5°) and was accounted for when taking measurements. So the value of the input angle where the peaks were measured was either 0° or 5° and 90° or 95°, and the input angle where noise was seen was at either 45° or 50°.

(48) Abel, S.; Eltes, F.; Ortmann, J. E.; Messner, A.; Castera, P.; Wagner, T.; Urbonas, D.; Rosa, A.; Gutierrez, A. M.; Tulli, D.; Ma, P.; Baeuerle, B.; Josten, A.; Heni, W.; Caimi, D.; Czornomaz, L.; Demkov, A. A.; Leuthold, J.; Sanchis, P.; Fompeyrine, J. Large Pockels Effect in Micro- and Nanostructured Barium Titanate Integrated on Silicon. Nature Mater, 2018, 18 (1), 42–47.

(49) Kim, I.-D.; Avrahami, Y.; Socci, L.; Lopez-Royo, F.; Tuller, H. L. Ridge Waveguide Using Highly Oriented $BaTiO_3$ Thin Films for Electro-Optic Application. Journal of Asian Ceramic Societies, 2014, 2 (3), 231–234.

(50) Lin, E. L.; Posadas, A. B.; Zheng, L.; Elliott Ortmann, J.; Abel, S.; Fompeyrine, J.; Lai, K.; Demkov, A. A.; Ekerdt, J. G. Atomic Layer Deposition of Epitaxial Ferroelectric Barium Titanate on Si(001) for Electronic and Photonic Applications. Journal of Applied Physics, 2019, 126 (6), 064101.

(51) Weis, R. S.; Gaylord, T. K. Lithium Niobate: Summary of Physical Properties and Crystal Structure. Appl. Phys. A, 1985, 37 (4), 191–203.

(52) Hamze, A. K.; Reynaud, M.; Geler-Kremer, J.; Demkov, A. A. Design Rules for Strong Electro-Optic Materials. npj Comput. Mater., 2020, 6 (1), 130.

(53) Edmondson, B. I.; Kwon, S.; Ortmann, J. E.; Demkov, A. A.; Kim, M. J.; Ekerdt, J. G. Composition and Annealing Effects on the Linear Electro-optic Response of Solution-deposited Barium Strontium Titanate. J. Am. Ceram. Soc., 2020, 103 (10), 5700–5705.